# Scattering States of Ionized Dopants Probed by Low Temperature Scanning Tunneling Spectroscopy

Chr. Wittneven, R. Dombrowski, M. Morgenstern,* and R. Wiesendanger
*Institute of Applied Physics, University of Hamburg, Jungiusstraße 11, D-20355 Hamburg, Germany*
(Received 17 March 1998)

*N* type InAs(110) is investigated by scanning tunneling spectroscopy at low temperature. $dI/dV$ images at positive sample bias exhibit circular corrugations, which are caused by the scattering of electron waves at the attractive potential of ionized dopants. Normalizing the images by simultaneously recorded constant current images gives quasidirect access to the surface distribution of the corresponding energy selected scattering states. The normalized images are in quantitative agreement with a WKB model. The energy dependence of the scattering cross section can be estimated from the model. [S0031-9007(98)08001-6]

PACS numbers: 71.20.Nr, 61.16.Ch, 72.10.Fk, 73.20.Hb

The scattering of electrons at ionized impurities determines the electrical conductivity of semiconductors at low temperatures and is important for the electron mobility in low dimensional quantum systems [1]. It seems worthwhile to study this process in detail. Scanning tunneling spectroscopy is an excellent tool for this purpose, since it combines high lateral and spectroscopic resolution. It allows us to study the spatial distribution of electronic states at selected energies around individual scatterers. The scattering of electron waves at step edges and impurities on metal surfaces has been studied by low temperature scanning tunneling microscopy (LTSTM) and spectroscopy (LTSTS) [2]. Here, we extend the method to semiconductors and investigate scatterers (ionized dopants) located several nm below the surface [3]. From the quantitative analysis of the imaged scattering states, we estimate the depth of the scatterer and deduce the energy dependence of the scattering cross section $\sigma(E)$.

The UHV-LTSTM apparatus described elsewhere [4] allows measurements down to 8 K in magnetic fields up to 7 T perpendicular to the surface. The noise level in topographic images is 0.03 Å and the achieved energy resolution is 6 meV [5]. Prior to measurements on InAs, the STM-tip (tungsten) is prepared on W(110) by applying voltage pulses (5 V, 10 ms) between tip and sample. *N*-doped InAs $[N_D = (2.0 \pm 0.1) \times 10^{16}\ \mathrm{cm}^{-3}]$ is cleaved *in situ* at a base pressure of $4 \times 10^{-11}$ mbar. The dopant concentration is checked by Hall measurements (4–300 K) and secondary ion mass spectroscopy revealing that the sample is degenerate and the main dopant is sulphur. After cleavage the sample is transferred into the precooled microscope, which itself is transferred into the cryostat. The STM-detected contamination of the sample is typically of the order of $1 \times 10^{-7}$ adsorbates/Å$^2$. Because of the low pressure inside the cryostat, it does not increase for several weeks. Topographic images $[z(x,y)]$ are recorded in constant-current mode, $dI/dV$ images are measured simultaneously by lock-in technique ($V_{\mathrm{mod}} = 8.5\ \mathrm{mV}_{pp}$). All measurements are performed at $8 \pm 1$ K.

Figure 1a shows a topographic image of clean *n*-InAs(110). It exhibits a number of bright spots with a height of up to 0.5 Å and a diameter of about 15 nm. The number of spots is nearly proportional to the dopant concentration as has been checked on highly doped *p*-InAs(110) ($N_A = 3 \times 10^{18}\ \mathrm{cm}^{-3}$). The bright spots are caused by the local band bending around ionized dopants [6]. The density of dopants appearing with a corrugation higher than 0.25 Å is $(1.2 \pm 0.2) \times 10^{-4}\ \mathrm{nm}^{-2}$. Consequently, these dopants are located up to 6 nm below the surface [7]. Besides the bright spots corrugations larger

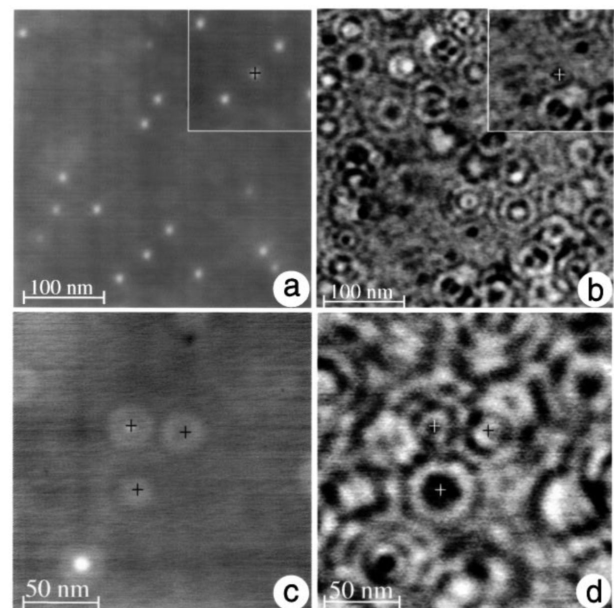


FIG. 1. (a) Topographic image of InAs(110), $V = 50$ mV ($V := V_{\mathrm{sample}}$), $I = 400$ pA; (b) $dI/dV$ image of the same surface area as in (a); $V = 50$ mV, $I = 400$ pA, $V_{\mathrm{mod}} = 8.5\ \mathrm{mV}_{pp}$; insets: 120 nm × 120 nm. (c) Topographic image of a surface region containing only dopants appearing lower than 0.2 Å, $V = 50$ mV, $I = 400$ pA; (d) $dI/dV$ image of the same surface area as in (c); $V = 50$ mV, $I = 400$ pA, $V_{\mathrm{mod}} = 8.5\ \mathrm{mV}_{pp}$; crosses mark corresponding positions.

 0031-9007/98/81(25)/5616(4)$15.00 © 1998 The American Physical Society

in diameter and weaker in height appear (Fig. 1c). The highest corrugation in Fig. 1c is 0.2 Å. Weaker corrugations are ascribed to deeper dopants. They exhibit an inner structure and a surrounding ring. Since the analysis of constant-current images is rather complicated [8], we recorded $dI/dV$ images simultaneously.

Figures 1b and 1d show the $dI/dV$ images corresponding to Figs. 1a and 1c. They exhibit a number of concentric ring structures, which are ascribed to standing electron waves around ionized dopants. There are more ring structures than features visible in topographic images. However, all topographic features are centers of ring structures in the corresponding $dI/dV$ image (see crosses marking corresponding positions). The insets in Figs. 1a and 1b demonstrate that the dopants appearing bright in topographic images appear dark in $dI/dV$ images. This is due to the increased tip-surface distance $z(x,y)$ above bright dopants resulting in a decreased transmission coefficient and a reduced $dI/dV$ signal. Obviously, the influence of $z(x,y)$ must be eliminated.

The relation between the measured $dI/dV(V,x,y)$ signal ($x,y$: surface position) and the energy resolved local density of empty states $\rho_{\mathrm{sample}}(E,x,y)$ [at low temperatures ($T \approx 0$ K) and tip-surface distances large enough to apply the transfer Hamiltonian formalism ($z \geq 4$ Å)], is given by [9] ($E_{\mathrm{F}} = 0$ eV):

$$\frac{dI}{dV}(V,x,y)|_{I=\mathrm{const}} \propto e\rho_{\mathrm{tip}}(0)\rho_{\mathrm{sample}}(eV,x,y)T(eV,V,z(x,y)) + \int_0^{eV}\left[\rho_{\mathrm{tip}}(eV-E)\rho_{\mathrm{sample}}(E,x,y)\frac{dT(E,V,z(x,y))}{dV}\right]dE + \int_0^{eV}\left[\frac{d\rho_{\mathrm{tip}}(eV-E)}{dV}\rho_{\mathrm{sample}}(E,x,y)T(E,V,z(x,y))\right]dE \tag{1}$$

[$\rho_{\mathrm{tip}}(E)$: tip density of states, $T(E,V,z)$: transmission coefficient]. Only $T(E,V,z)$ depends on $z(x,y)$ [9]. At low sample voltages $T(z)$ is directly proportional to $I(z)$. Therefore, we can eliminate the influence of $z(x,y)$ by measuring $I(z)$ with the tip used for $dI/dV$ images. The measured $I(z)$ at sample voltages below 300 mV can be fitted for a $z$ range of more than 4 Å by [10]

$$I(z) \propto \exp[-\sqrt{\Phi - eV/2}\,z]. \tag{2}$$

The $I(z)$ curves above dopants appearing less high than 0.2 Å differ only slightly from the curves above the flat surface ($\Delta\Phi/\Phi \leq 4\%$) [10]. Here, we restrict the discussion to dopants appearing lower than 0.2 Å.

We insert the measured $z(x,y)$ (topographic images) in $I(z)$ [Eq. (2)] and find:

$$\frac{\frac{dI}{dV}(V,x,y)}{I[z(x,y)]} \propto \rho_{\mathrm{sample}}(eV,x,y) + \dots. \tag{3}$$

This relation allows us to extract $\rho_{\mathrm{sample}}(E,x,y)$ directly from measured data [11]. The uncertainty of the method is given by the two additional terms from Eq. (1). From the knowledge of $T(eV,V,z)$ [Eq. (2)] one concludes that the second term is less than 5% of the first term ($V \leq 200$ mV). The third term depends on $\frac{d\rho_{\mathrm{tip}}}{dV}\frac{V}{\rho_{\mathrm{tip}}}$, which can be considred to be small, since we find no indications of sharp tip structures ($\frac{d\rho_{\mathrm{tip}}}{dV}$) in $dI/dV$ curves [10]. In summary, the error bar of the method can be estimated to be less than 10%.

$dI/dV$ images of one concentric ring structure recorded at different energies are shown in the first row of Fig. 2. The size and the relative intensity of adjacent rings does not depend on the tip-surface distance, but only on $V_{\mathrm{sample}}$. With increasing voltage the size of the rings shrinks and the signal to noise ratio decreases. The second row shows the normalized $(dI/dV)/I(z)$ images, which are proportional to $\rho_{\mathrm{sample}}(eV,x,y)$ [Eq. (3)]. The trends of the first row persist, but the size of the rings as well as their intensity relation has been changed. An offset is subtracted from the images 2(a1)–2(b7) to optimize the contrast of the ring structure. Only about 5% of the $(dI/dV)/I(z)$ signal is corrugated.

Next, we show that the corrugations of $\rho_{\mathrm{sample}}$ are due to electron scattering states of the attractive potential of ionized dopants. Their expected surface distribution can be estimated by a WKB model [12]. The electric potential consists of the dopant potential and the tip induced band bending [13]. From this the squared wave function of the scattering state at different energies can be deduced. The value directly below the actual tip position $(x,y)$ corresponds to $\rho_{\mathrm{sample}}(x,y)$. Each $(x,y)$ has to be considered separately.

The attractive Coulomb potential of the dopant is taken as $V(r) = e/4\pi\varepsilon_r\varepsilon_0 r$ ($r$: distance from dopant; $\varepsilon_0$: dielectric constant in vacuum; $\varepsilon_r = 14.5$: dielectric constant of InAs [14]). It is checked that screening effects are of minor importance. The tip induced potential is calculated by twofold numerical integration of the Poisson equation [13]. The work function difference between sample and tip $\Delta\Phi_{\mathrm{st}}$ and the lateral extension of the tip induced potential $\phi_{\mathrm{QD}}$ have to be known. The values are estimated as described in [15] by analyzing the $dI/dV$ spectrum of the tip induced quantum dot. The analysis of the tip used in Figs. 1 and 2 results in $\Delta\Phi_{\mathrm{st}} = 160$ meV and $\phi_{\mathrm{QD}} = 150$ nm. Figure 3 shows a 3D sketch of the resulting potential caused by the presence of the tip and an ionized dopant.

Next, we calculate the wave function of the scattering state. A reasonable good approximation is to use

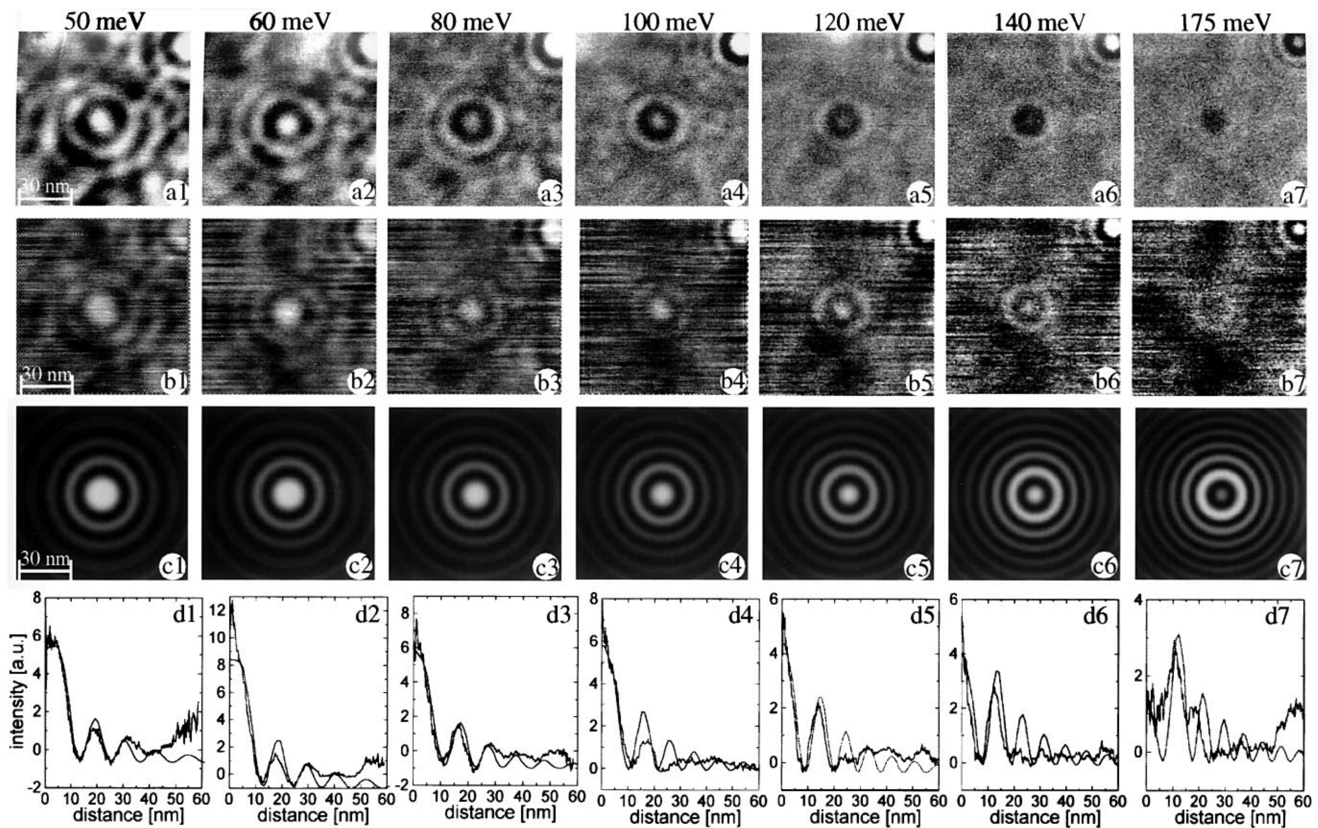


FIG. 2. (a1)–(a7): $dI/dV$ images measured at sample voltages indicated above, $I = 400$ pA, $V_{\mathrm{mod}} = 8.5$ mV$_{pp}$; (b1)–(b7): $(dI/dV)/I(z)$ images corresponding to (a1)–(a7); (c1)–(c7): Simulated surface distribution of scattering states of an ionized dopant ($z_D = 14.3$ nm); energies of the scattering state correspond to the voltages marked above (a1)–(a7); (d1)–(d7): Comparison of circular line sections of (b1)–(b7) and (c1)–(c7). (A circular line section represents the average intensity on a circle of constant distance from the center of the rings.); smoother curves belong to simulated images.

spherical coordinates $(r, \Theta, \varphi)$ and separate the Schrödinger equation with respect to the $r$ coordinate. We apply the WKB method along $r$ (straight lines from the dopant to the surface). $E_{\mathrm{CBM}}(r)$ shown in Fig. 3 defines the local potential. It is smooth enough to apply the WKB method (except very close to the dopant). The local wavelengths $\lambda(E, r)$ are calculated corresponding to the nonparabolic $E(\mathbf{k})$ dispersion of InAs. Phase coherence is preserved by integrating the wave function phase of the scattering state $\varphi(r)$ stepwise starting from the center of the dopant. The bottom of Fig. 3 shows $\sin^2[\varphi(r)]$ for an electron energy $E - E_{\mathrm{F}} = 50$ meV and a tip position $(x, y) = (0, 0)$. Taking into account that $\rho_{\mathrm{sample}}^{\mathrm{scatt}}(r)$ (the squared amplitude of the wave function) is proportional to $(1/r^2)\sin^2[\varphi(r)]$, we can determine the spatially varying contribution of $(dI/dV)/I(z)$ for each $(x, y)$. Notice that it remains only one parameter to fit size, energy dependence, and intensity relations of the concentric ring structures: The depth of the dopant below the surface ($\mathbf{z_D}$). This might justify the rather crude approximations of the calculation [16].

The best fit for the images of the second row of Fig. 2 is shown in the third row and obtained for $z_D = 14.3$ nm. To compare model and experiment more quantitatively,

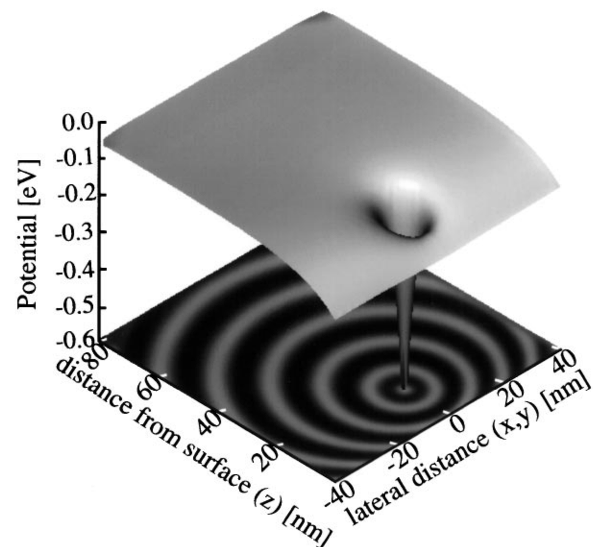


FIG. 3. 3D image: Calculated potential caused by an ionized dopant ($z_D = 14.3$ nm) and the tip induced band bending ($\Delta\Phi_{\mathrm{st}} = 160$ meV); the lateral extension $(x, y)$ of the tip induced potential ($\phi_{\mathrm{QD}} = 150$ nm) is not visible; the $z$ direction points into the sample. 2D image: $\sin^2(\varphi)$ distribution of the resulting scattering state at $E - E_{\mathrm{F}} = 50$ meV. (See text for discussion.)

the fourth row of Fig. 2 presents circular line sections of the experimental and calculated images. The agreement is rather good.

To check the correctness of the fit parameter $z_D$, the described procedure is applied to the 10 best visible ring structures of Fig. 1d (200 nm $\times$ 200 nm). The resulting $z_D$ of the dopants appear to be distributed in a $z$ slice of 20 nm. This would imply $N_D = 1.25 \times 10^{16}$ cm$^{-3}$, a value lower than the real dopant concentration. The difference is mainly caused by the fact that some patterns could not be analyzed. They overlap too strongly with neighboring features. Notice that about 15 (and not 10) ring structures appear in Fig. 1d. However, also the approximations discussed above might influence the resulting $z_D$ values.

An exact knowledge of $z_D$ would allow one to determine the reflective scattering cross section $\sigma_R(E)$ of individual dopants by comparing the amplitude of the corrugations with the average signal in $(dI/dV)/I(z)$ images. But, even without the exact knowledge of $z_D$, $\sigma_R(E)$ can be given in arbitrary units (not depending on $z_D$) as shown in Fig. 4 for the dopant analyzed in Fig. 2. A trend of decreasing $\sigma_R$ with increasing $E$ in qualitative agreement with scattering theory is found. The data are compatible with a $1/E^2$ fit as expected from the Born approximation, but a $1/E$ fit seems more appropriate. We emphasize that the determination of the reflective scattering cross section does not depend on the tip density of states. This influence is eliminated by the division of the corrugated signal by the average signal.

In summary, we have studied the scattering of electron waves at attractive ionized dopants in detail by scanning tunneling spectroscopy. A WKB model of the scattering states, using the depth of the dopants below the surface as a fitting parameter, reproduces size, intensity relation,

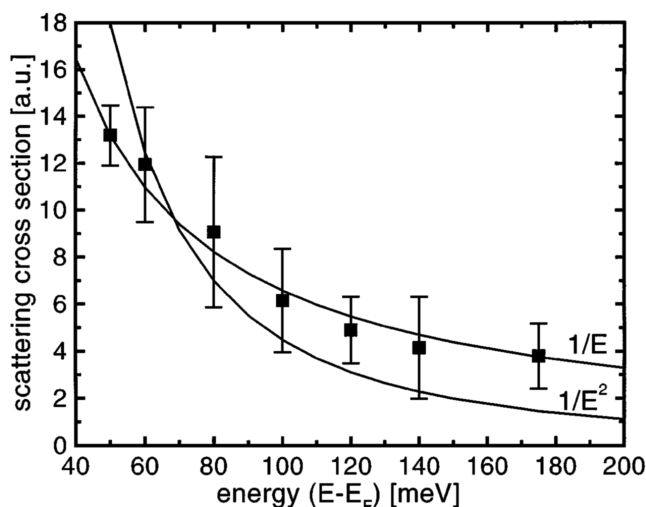


FIG. 4. Reflective scattering cross section of the dopant analyzed in Fig. 2. Assuming a depth of the dopant $z_D = 14.3$ nm the $y$ scale would be in nm$^2$. The lines show $1/E$ and $1/E^2$ curves for comparison.

and energy dependence of the surface corrugations found in $(dI/dV)/I(z)$ images $[\propto \rho_{\mathrm{sample}}(x,y)]$. The depths of the dopants calculated from comparison of model and experiment are slightly larger than expected from the dopant concentration. It is shown that an exact knowledge of the depth allows the direct measurement of reflective scattering cross sections of individual dopants.

We are grateful to W. Hansen and U. Merkt for helpful discussions. Financial support by the DFG through SFB 508 and the Graduiertenkolleg "Physik nanostrukturierter Festkörper" is gratefully acknowledged.

*Author to whom correspondence should be addressed.

[1] T. Ando *et al.,* Rev. Mod. Phys. **54**, 437 (1982); W. Rauch *et al.,* J. Appl. Phys. **70**, 6860 (1991); F.G. Pikus, Sov. Phys. Semicond. **25**, 439 (1991); K. Ishibashi *et al.,* J. Appl. Phys. **32**, 6246 (1993); T. Suski *et al.,* Solid State Electron. **37**, 6246 (1994).

[2] M.F. Crommie *et al.,* Nature (London) **363**, 524 (1993); E.J. Heller *et al.,* Nature (London) **369**, 464 (1994); Y. Hasegawa *et al.,* Phys. Rev. Lett. **71**, 1071 (1993); Ph. Avouris *et al.,* Science **264**, 942 (1994); Ph. Avouris *et al.,* Chem. Phys. Lett. **240**, 423 (1995); Ph. Hoffmann *et al.,* Phys. Rev. Lett. **79**, 265 (1997).

[3] Electronic structures due to tip induced bound states around dopants have been observed by M.C.M.M. van der Wielen *et al.,* Phys. Rev. Lett. **76**, 1075 (1996).

[4] Chr. Wittneven *et al.,* Rev. Sci. Instrum. **68**, 3806 (1997).

[5] R. Dombrowski *et al.,* Appl. Phys. A **66**, 203 (1998).

[6] M.B. Johnson *et al.,* Appl. Phys. Lett. **63**, 2923 (1993); J.F. Zheng *et al.,* Phys. Rev. Lett. **72**, 1490 (1994); P. Ebert *et al.,* Phys. Rev. B **53**, 4580 (1996); T. Trappmann *et al.,* Europhys. Lett. **38**, 177 (1997); M. Morgenstern *et al.,* Phys. Status Solidi (to be published).

[7] The dopant concentration can be assumed to be isotropic up to the surface, since $S$ donors are immobile at room temperature; see E. Schillmann, *Compound Semiconductors—Preparation of III-V Compounds,* edited by R.K. Willardson and H.L. Goering (Reinhold, New York, 1962), Vol. 1, p. 358.

[8] J.A. Stroscio *et al.,* J. Vac. Sci. Technol. B **6**, 1472 (1988).

[9] J. Bardeen, Phys. Rev. Lett. **6**, 57 (1961); J. Tersoff *et al.,* Phys. Rev. B **31**, 805 (1985); for a review, see J.A. Stroscio and W.J. Kaiser, *Scanning Tunneling Microscopy* (Academic Press, San Diego, 1994).

[10] Chr. Wittneven, Ph.D. thesis, Hamburg, 1998; R. Dombrowski, Ph.D. thesis, Hamburg, 1998.

[11] A similar argument is given in J. Li *et al.,* Phys. Rev. B **56**, 7656 (1997).

[12] See, e.g., F. Schwabl, *Quantenmechanik* (Springer, Berlin, 1988), p. 183.

[13] R.M. Feenstra *et al.,* J. Vac. Sci. Technol. **5**, 923 (1987).

[14] C. Hilsum and A.C. Rose-Innes, *Semiconducting III-V Compounds* (Pergamon, New York, 1961).

[15] R. Dombrowski *et al.,* Phys. Rev. B (to be published); J. Wildöer *et al.,* Phys. Rev. B **55**, 16013 (1997).

[16] A detailed discussion of the approximations will be published elsewhere.